

Rapid estimation of synthesizability windows of inorganic materials from first principles

Finja Tadge,¹ Javier Sanz Rodrigo,¹ and Andrea Crovetto^{1,*}

¹*National Centre for Nano Fabrication and Characterization (DTU Nanolab),
Technical University of Denmark, 2800 Kongens Lyngby, Denmark*

Fast prediction of the synthesizability conditions of materials remains challenging, even assuming synthesis under thermodynamic equilibrium. Approaches solely based on convex stability hulls neglect finite-temperature effects, while phonon-based phase diagram calculations are computationally demanding. Here, we demonstrate high-throughput generation of phase predominance diagrams as a function of temperature and partial pressures of gaseous reactants, helping bridge the gap between computational predictions and experimental synthesis. We employ fitting of elemental phase reference energies to zero-temperature total energies for improved calculation of formation enthalpies, along with machine-learned interatomic potentials for rapid determination of vibrational entropy and heat capacity. The resulting predominance diagrams can be intuitively understood by experimentalists and can be used to translate energies above stability hulls into synthesis conditions. Predominance diagrams are generated for selected oxide, nitride, sulfide, and phosphide systems, as well as for 48 more complex ternary metal phosphosulfide systems. The calculated predominance diagrams generally show good agreement with the experimental synthesis literature, with a drastic reduction in computational cost compared to a conventional approach relying on DFT-based phonon calculations. We identify several compounds predicted to be stable under well-defined thermodynamic windows, even though they appear as metastable in a zero-temperature stability hull picture. The method can be applied to rapidly estimate synthesis conditions for any inorganic material.

I. INTRODUCTION

The energy above the zero-temperature convex stability hull E_h is often employed as a metric for assessing the synthesizability of compounds [1, 2]. While E_h has traditionally been calculated with density functional theory (DFT), crystal-graph attention neural network models have now extended the assessment of thermodynamic stability to the range of 10^9 materials. [3]. However, such zero-temperature approaches do not necessarily reflect realistic temperature- and pressure-dependent synthesis conditions.

Accurate computational phase diagrams at finite temperatures and pressures require explicit modeling of the temperature-dependent heat capacity of materials and of the entropic contributions to their Gibbs free energy. Phonon calculations are needed to determine heat capacities and vibrational entropy [4]. Total energy calculations on a large number of structures generated by quasi-random [5] or Monte Carlo sampling [6] are commonly employed to estimate configurational entropy. These methods are computationally expensive and unsuitable for large-scale, high-throughput phase diagram prediction.

Less costly alternatives, including machine learning-based descriptor approaches for Gibbs free energy prediction, have been proposed [7]. While useful, descriptor-based methods are intrinsically heuristic and may not generalize well to material systems beyond the training set. Similarly, machine learning models trained

on text-mined synthesis recipes have so far shown limited generalizability for predicting experimental synthesis conditions [8] and a tendency to overestimate the likelihood of synthesis [9]. Consequently, large-scale, high-throughput synthesizability prediction across complex phase spaces under realistic experimental conditions remains a major challenge.

With the recent emergence of machine-learned interatomic potentials (MLIPs), the first low-cost workflows to integrate physics-based entropy contributions to the Gibbs free energy of materials have been proposed [10–12]. These initial reports have focused on systems where configurational entropy is dominant, such as solid solutions of metals and of gapped solids [10] and high-entropy alloys [11]. There are at least still three open questions.

First, can MLIP-based methods produce high-throughput phase diagrams of nominally ordered inorganic materials of usable quality to inform experimental synthesis? For these materials it is important to include vibrational energy and heat capacity, but it may be acceptable to neglect configurational entropy, which is more costly to calculate even with MLIPs. [11]

Second, can the latest generation of MLIP foundation models significantly improve predictive power in materials thermochemistry over its predecessors? In particular, the MatterSim MLIP foundation model [13] has very recently been shown to perform particularly well at phonon calculations in a benchmark study [14]. Due to its accuracy at predicting the maximum phonon frequency and phonon density of states (DOS), MatterSim gives mean absolute errors of only 15 J/(mol·K) in vibrational entropy and 3 J/(mol·K) in heat capacity at constant volume with respect to explicit DFT calculations at the PBE level.

* ancro@dtu.dk

Third, can we present high-throughput calculated phase diagrams in a way that is intuitively understood by experimental synthesis scientists? MLIP-generated phase diagrams for metallic solid solutions have been plotted as a function of temperature and metal composition, [10, 11]. Calculated phase diagrams of compounds have traditionally been plotted as a function of temperature and atomic chemical potentials [7]. From the perspective of an experimentalist, the synthesizability windows of materials that are grown through solid/gas-phase reactions are easiest to visualize as a function of reactive gas partial pressure rather than chemical potentials [15].

In this work we address the questions above, leveraging recent advances in universal MLIPs [14] to enable high-throughput generation of phase diagrams of ordered inorganic materials as a function of temperature and partial pressures of the reactive gases.

In a first step (Fig. 1), DFT calculations are used to compute enthalpies at zero temperature, with the accuracy of formation energies improved using the fitted elemental reference energies (FERE) approach [16]. Subsequently, the MatterSim MLIP foundation model [13] is employed for rapid phonon band structure calculations to determine vibrational entropies and heat capacities. This calculation step takes just a few minutes on a standard compute node, thus circumventing the bottleneck of DFT phonon calculations in computational thermochemistry. From this information, the Gibbs free energies of all compounds, are computed as a function of temperature and gas-phase chemical potentials using standard thermochemical relationships. The resulting phase predominance diagrams can be conveniently represented in two dimensions of choice for intuitive understanding by experimentalists looking to synthesize the materials. Combining ab-initio DFT calculations, MLIPs and standard thermochemistry provides a physics-based workflow that can conveniently be extended to include different compound classes across the periodic table.

We evaluate the chemical versatility of this workflow by generating phase diagrams in four chemically diverse binary systems (oxides, nitrides, sulfides, phosphides) and comparing them to experiment. As a high-throughput application of this method, we generate phase diagrams for 48 distinct metal phosphosulfide ternary systems, comprising over 1000 ternary compounds and about 450 binaries, and including 19 new materials that we recently found to lie on the 0 K stability hull [17]. The predicted windows of thermodynamic stability show promising agreement with available experimental synthesis conditions for bulk materials, highlighting the potential of this approach for high-throughput prediction of synthesis conditions of computationally discovered materials.

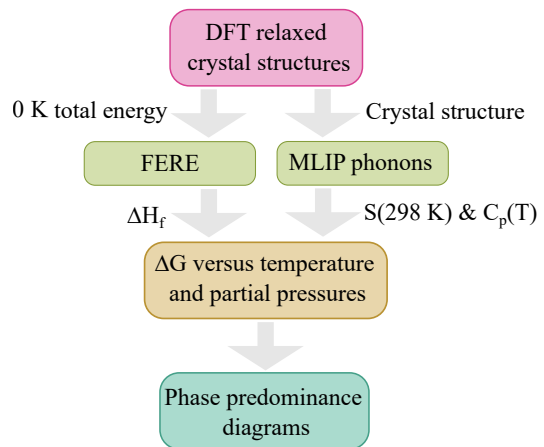


FIG. 1. Workflow for high-throughput calculation of thermodynamic stability windows of materials versus temperature and partial pressures. Phase predominance diagrams are constructed based on the formation enthalpy ΔH_f , vibrational entropy $S(298\text{ K})$ and heat capacity C_p calculated by combining DFT with the FERE approach and MLIP phonon calculations.

II. RESULTS

A. Binary systems: Oxides, nitrides, sulfides, phosphides

1. Errors and uncertainty

Phase predominance diagrams showing compound stability regions as a function of temperature and partial pressure of the reactant gas are constructed for four chosen binary systems in the oxide, nitride, sulfide and phosphide families (Fig. 2). The specific binary systems (V-O, Ta-N, Sn-S, and Cu-P) were chosen as they contain a large number of experimentally known crystalline compounds relative to other binary systems their respective family. The diagrams are based on the Gibbs free energy calculated from the formation enthalpy ΔH_f , entropy S , and constant-pressure heat capacity C_p of each compound. The procedure used to calculate these thermodynamic quantities is described in detail in the Methods section. Experimental values of S and C_p at room temperature ($S(298\text{ K})$, $C_p(298\text{ K})$) for a reference dataset containing 389 binary oxides, nitrides, phosphides and binary, ternary and quaternary sulfides, are reproduced with MAEs of $0.042\text{ meV}/(\text{atom}\cdot\text{K})$ and $0.043\text{ meV}/(\text{atom}\cdot\text{K})$, respectively (see Fig. 3). It is important to note that the experimentally available entropy data includes all sources of entropy including configurational. The relatively low error in the entropy calculated via MLIP phonons implies that considering only vibrational entropy in crystalline, non-alloyed compounds is a reasonable assumption.

The accuracy of DFT-calculated formation enthalpies compared to experimentally measured values is improved

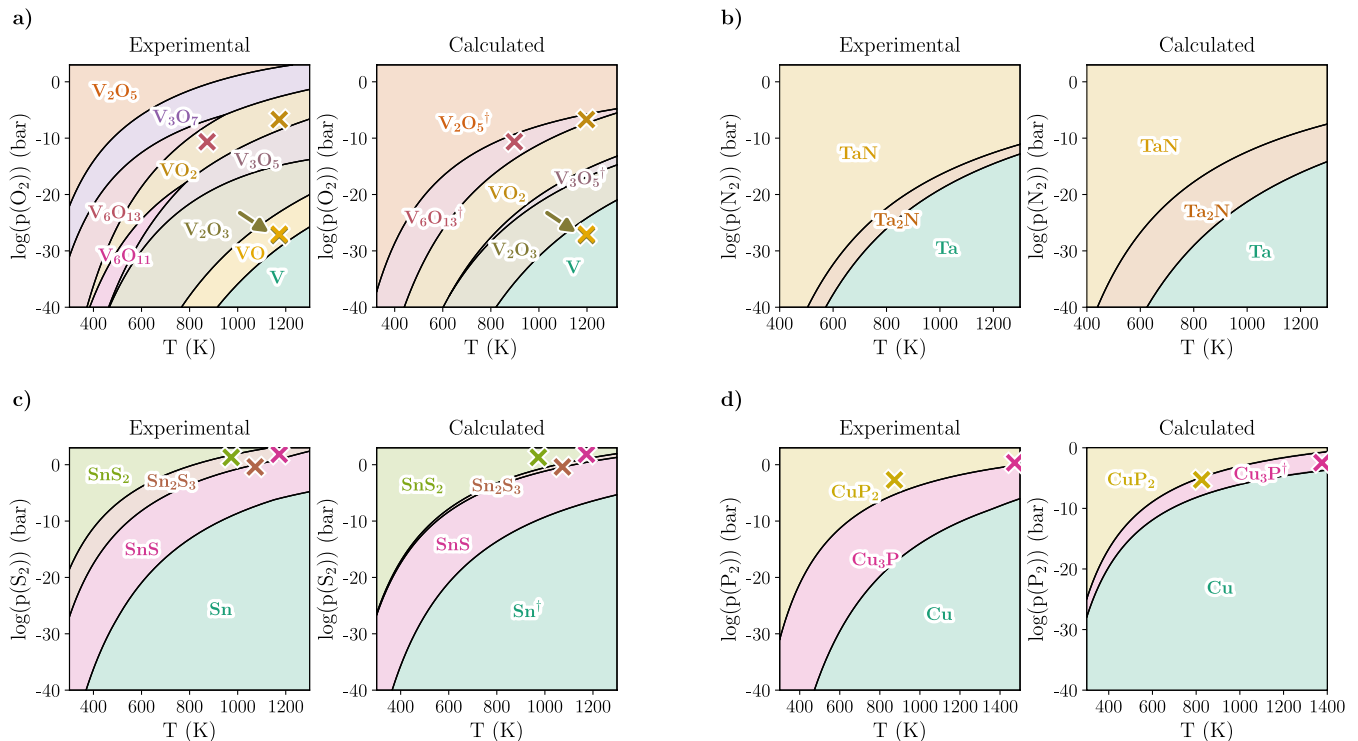


FIG. 2. Exemplary phase predominance diagrams constructed for the V-O, Ta-N, Sn-S and Cu-P binary systems based on both experimentally measured and computationally derived thermodynamic properties. Only binaries that are present in both the experimental and the computational database are considered here. Stability regions are color-coded by compound, with labels displayed in matching colors. All phases exhibiting imaginary frequencies according to MLIP phonon band structures are marked with a dagger (\dagger), indicating potential dynamic instability [18]. Synthesis conditions for experimentally reported compounds are marked with a cross in a color representing the corresponding composition [19–24]. The derivation of gas partial pressures from the reported synthesis conditions is detailed in the SI. Literature synthesis conditions for V_2O_3 and VO coincide and are thus marked with an additional arrow.

by introducing a fitted correction to the elemental reference phase energies (FERE) [16]. Separate corrections are fitted for the oxide (150 compounds) and sulfide (118 compounds) binary systems. Due to the limited availability of experimental formation enthalpies for nitrides and phosphides, one common set of corrections is fitted to the phosphide-nitride set (98 pnictide compounds). The fitting scheme and results are detailed in the Methods section. MAEs between the experimental and computational formation enthalpy are 0.236 eV/atom (O), 0.204 eV/atom (S) and 0.160 eV/atom (N-P). After the FERE corrections, the MAEs are reduced to 0.069 eV/atom, 0.058 eV/atom and 0.055 eV/atom, respectively (see Table I and Fig. 4). For reference, a common estimate for the error of experimentally measured formation enthalpies is 0.040 meV/atom [25].

It follows that the error on the formation enthalpy generally dominates over the heat capacity and entropy errors. It is only at temperatures above 1000 K that they become comparable. Hence the overall accuracy of our calculated phase predominance diagrams is primarily limited by the accuracy of the formation enthalpy prediction, even though this prediction is DFT-based rather

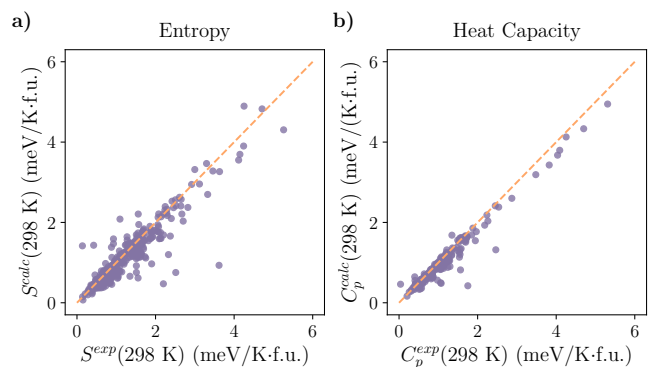


FIG. 3. MLIP calculated values of $S(298\text{ K})$ and $C_p(298\text{ K})$ in meV/(K-formula unit) compared to experimental values for all binaries considered in the different datasets.

than MLIP-based. This is an important conclusion, as it demonstrates that MLIP phonons with the MatterSim model are not the factor limiting the accuracy of calculated phase diagrams.

Dataset	N	n_{el}	MAE ΔH_f (eV/atom)	MAE ΔH_f^{FERE} (eV/atom)
Binary oxides	150	74	0.236	0.069
Binary sulfides	118	68	0.204	0.058
Binary nitrides and phosphides	98	53	0.160	0.055
Binary and ternary phosphides and sulfides	144	50	0.158	0.072

TABLE I. Corrections to the elemental reference-phase energies are fitted for three different datasets. N describes the number of compounds considered in the fitting and n_{el} corresponds to the number of elements whose reference-phase energies are corrected. MAEs for the formation enthalpy before (ΔH_f) and after (ΔH_f^{FERE}) fitting are reported.

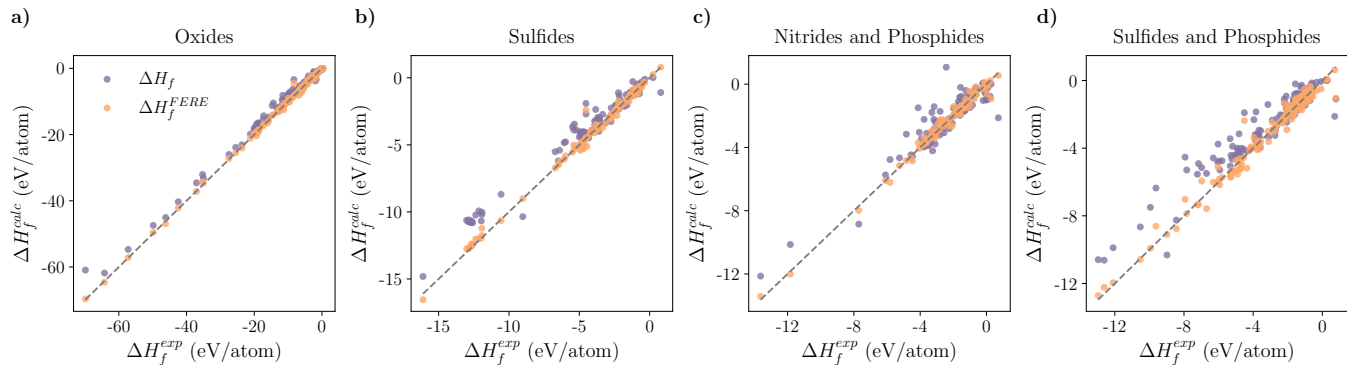


FIG. 4. Values of ΔH_f^{calc} obtained with the FERE method compared to uncorrected values for the three considered datasets. A calculation of ΔH_f^{calc} based on eq. 1 without fitted elemental corrections leads to a significant overestimation of ΔH_f^{calc} for the majority of the compounds in the O-, S- and P-S- dataset. Agreement with experimental values ΔH_f^{exp} is significantly increased when including the FERE energies in the formation enthalpy calculation.

2. Comparison with experiment

To assess the impact of these uncertainties on the predicted phase predominance diagrams, phase boundaries derived using the workflow presented in this work are compared to phase diagrams constructed solely from experimental thermochemical data. Only compounds included in both our chosen experimental thermochemical database (HSC Chemistry [26]) and our chosen computational database of DFT formation enthalpies (Ref. [27] plus additional structures taken from either Materials Project [1] or ICSD [28] and relaxed by us) are considered. Fig. 2 shows experimental and calculated phase predominance diagrams for the V-O, Ta-N, Sn-S and Cu-P binary systems. All phase diagrams are presented as a function of temperature and partial pressure of a relevant gaseous source for the respective anion (O_2 , N_2 , S_2 , P_2). In general, good agreement between the predicted and experimental phase boundaries is observed for all four binary systems. The majority of the experimentally synthesized phases are not only reproduced but also predicted stable under similar windows of gas partial pressures and temperatures in the experimental and computational thermochemical approaches.

It is interesting to see that temperature- and pressure-dependent thermodynamic modeling reveals stability

windows for compounds that would be classified as metastable from a typical zero-temperature energy above hull approach. For example, two binary V-O compounds that have been experimentally synthesized (V_3O_5 and V_6O_{11}) lie slightly above the zero-temperature stability hull (E_h of 0.08 eV/atom and 0.05 eV/atom, respectively). Nevertheless, they are predicted to be stabilized over a broad range of temperatures by our computational approach. In the Cu-P binary system, Cu_3P is predicted to be thermodynamically stable at finite temperatures despite lying 27 meV/atom above the zero-temperature stability hull. This result explains why Cu_3P often forms more easily than CuP_2 [29] despite its zero-temperature metastability, as previously hypothesized [30]. These cases highlight the improved predictive capability of the presented approach for compound stability under realistic temperature and pressure conditions compared to zero-temperature stability metrics alone.

Uncertainties in the derived thermodynamic quantities lead primarily to shifts in the locations of phase boundaries resulting in an increase or a reduction of the stability window size for given compounds as observed for, e.g., Ta_2N and Sn_2S_3 in the calculated phase predominance diagrams. In some cases, an interplay of increase and reduction of stability window sizes for neighboring compounds can lead to single phases disappearing from

the phase predominance diagrams as it is the case for V_3O_7 , VO and V_6O_{11} in the phase diagram calculated for the V-O binary system.

For all phase boundaries included in Fig. 2, the error in the temperature of calculated phase boundary positions versus experiment is 270 K (MAE). The Sn-S and Cu-P systems have the lowest and highest MAE, respectively (140 K and 520 K). The procedure used to calculate these errors is detailed in the SI. These errors imply that experimentalists seeking to synthesize a compound can fix the gas partial pressure and choose a temperature in the middle of the predicted stability region of the targeted compound. If the temperature range of compound stability at that partial pressure is wider than $2 \times$ MAE (this is the case for many of the compounds in Fig. 2), then it is very likely that the chosen synthesis conditions fall in the real thermodynamic stability window of that compound. This gives a very practical criterion for evaluating the accuracy of our method.

It should also be noted that the experimental predominance diagrams in Fig. 2 are not generated based on direct observation of stability windows of different compound. Instead, they are based on experimental measurements of thermochemical properties of compounds, and are therefore indirect. The ultimate test of the correctness of a predominance diagram is comparison with experimentally reported synthesis conditions, marked by crosses in Fig. 2. Surprisingly, the agreement between stability windows and actual synthesis conditions is slightly better with our computationally determined phase predominance diagrams than with the experimental diagrams. Four synthesized compounds fall within the computationally predicted stability windows (V_6O_{13} , SnS_2 , Sn_2S_3 , Cu_3P). Four additional compounds (VO_2 , V_2O_3 , SnS and CuP_2) are reasonably close (50 K to 200 K off). This implies that the above-mentioned 270 K error for the phase boundary position is probably overestimated due to inaccuracies of the experimental benchmark.

3. Predictive power

After assessing our method’s limitations and its performance against experimental data, we now turn to using it as a predictive tool to identify synthesis conditions for new materials. We therefore construct a new set of predominance diagrams (Fig. 5) by considering all materials that are present either on Materials Project or the ICSD database, even if they have no associated thermochemical data. This includes compounds that have not been synthesized before. The V-O system is expected to be particularly challenging, since V has a tendency for both mixed valence and magnetic ordering. Overall, we considered 28 V-O binaries and predict stability windows for 7 of them (all true positives). V_7O_3 and V_8O are additions with respect to Fig. 2, and we correctly predict finite stability windows for both. However, such windows

occupy a region that was previously assigned to V_2O_3 , such that experimental synthesis conditions are no longer reproduced in the purely computational phase predominance diagram. In addition, there are 12 other V-O compositions that have been synthesized but do not appear in the predominance diagram (false negatives). We speculate that this is due to a combination of the complexity of V chemistry (see above) and the long history of synthesis in binary oxide systems, making it more likely that non-equilibrium routes have been found for the synthesis of thermodynamically unstable compounds. Under this assumption, one could argue that the earliest reported vanadium oxides are likely to be the ones with finite windows of thermodynamic stability, because they are more easily synthesized without the need to develop special reaction pathways for kinetic stabilization.

Indeed the four V-O binaries present in the ICSD that were reported before 1950 (VO_2 , V_2O_3 , V_2O_5 and V_6O_{13}) all exhibit finite windows of thermodynamic stability in the computational phase predominance diagram in Fig. 5. This indicates that the high occurrence of false negatives is not necessarily a flaw in the calculated diagrams, but may instead be a result of substantial efforts in the synthesis of metastable compounds in well-known materials systems.

For construction of the Ta-N predominance diagram in Fig. 5, 12 binaries are considered. The resulting diagram is extended by Ta_2N_3 and Ta_5N_6 , as well as Ta_3N_5 , Ta_4N_5 at high N_2 partial pressures, as compared to the diagram shown in Fig. 2. Ta_2N , TaN , Ta_3N_5 , Ta_4N_5 and Ta_5N_6 have been synthesized, while Ta_2N_3 has not, giving 5 true positives and 1 potentially synthesizable new material. 2 additional Ta-N binaries have been experimentally reported and do not appear in the presented phase predominance diagram (2 false negatives).

Although two additional theoretical phases (Sn_3S and Sn_3S_7) are included in the construction of the Sn-S phase predominance diagram, neither of these two binaries is predicted to be stabilized under the conditions considered in this work. For this system, all three phases present in the phase predominance diagrams are experimentally reported. Nevertheless, two additional synthesized Sn-S binaries (Sn_3S_4 and Sn_3S_7) do not appear, giving 3 true positives and 2 false negatives.

For the Cu-P binary system, a total of 10 binaries are considered for the construction of the phase predominance diagram leading to significant differences as compared to the diagram shown in Fig. 2. All four experimentally reported Cu-P binaries (CuP_2 , CuP_{10} , Cu_2P_7 and Cu_3P) appear in the presented phase predominance diagram. The new phase Cu_2P is predicted to be stabilized across all temperatures, resulting in 4 true positives, zero false negatives, and 1 potentially synthesizable new material for this binary system. The inclusion of other binaries compared to Fig. 2 leads to a significant reduction in the CuP_2 stability region. Nevertheless, the experimental synthesis conditions for Cu_3P are still accurately reproduced and the synthesis conditions for CuP_2 lie rea-

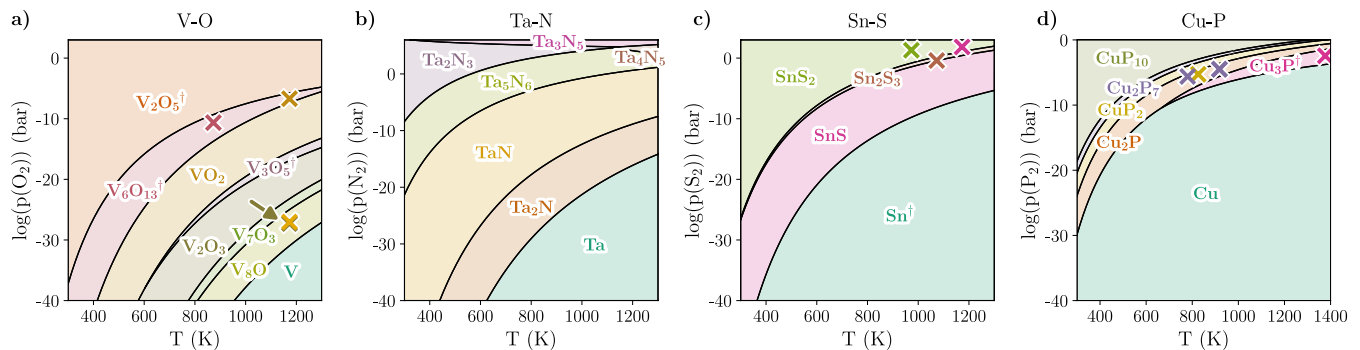


FIG. 5. Phase predominance diagrams constructed for the V-O, Ta-N, Sn-S and Cu-P binary systems based solely on calculated thermodynamic properties. Here, all experimentally or theoretically reported binary phases on Materials Project and the ICSD are considered, extending the diagrams to more materials than the ones with available experimental thermochemical data shown in Fig. 2. Experimental synthesis conditions are marked with a cross [19–24, 31]. See caption of Fig. 2 for further details.

sonably close to the new phase boundary.

B. Ternary systems with two gas-phase element sources: Phosphosulfides

1. High-throughput predominance diagrams

As a second case study, we show that our proposed method can readily be scaled to more than 1000 materials, even in the more complex case of multinary systems where two elements are supplied from the gas phase. The chemical space of interest is ternary metal phosphosulfides including (almost) all metals from the s, p and d-block. In this space, approximately 60% of the experimentally reported compounds lie on the zero-temperature convex hull ($E_h = 0$) [17]. This suggests that zero-temperature thermodynamic stability is a more useful descriptor of synthesizability in phosphosulfides than in, e.g., oxides and nitrides [34]. Nevertheless, a number of experimentally realized compounds, such as $CrPS_4$ ($E_h = 0.03$ eV/atom) [35], Cu_7PS_6 ($E_h = 0.05$ eV/atom) [36] or even $FePS_3$ with $E_h = 0.18$ eV/atom [37], lie above the zero-temperature stability hull and would therefore be classified as metastable within a 0 K framework.

In the SI, we show phase predominance diagrams for 48 distinct metal phosphosulfide ternary systems, comprising over 1000 ternary compounds and about 450 binaries. A large fraction of these materials are hypothetical unsynthesized compounds, 19 of which lie on the 0 K convex hull [17]. Similar to the binary systems, the accuracy of DFT-calculated formation enthalpies compared to experimentally measured values is improved by employing the FERE method. Since ternary phosphosulfides are absent from our experimental thermochemical database (HSC Chemistry), we apply the FERE method to 144 materials that are either phosphides (39) or sulfides (107), most of them binaries. With this approach, the MAE of the calculated formation enthalpy compared to experimen-

tally measured values is reduced from 0.158 eV/atom to 0.072 eV/atom. Since the errors of MLIP calculations of entropy and heat capacity are about 0.04 meV/(atom·K) (see above), using MLIP rather than DFT to calculate these quantities is not the dominant source of inaccuracy at temperatures below ~ 1500 K.

The average time needed for the high-throughput calculations is around 30 core-minutes per material for the DFT structure relaxation and additional 5 core-minutes per material for the MLIP phonon band structure and DOS. This time includes calculation of the derived thermochemical properties. Thus, MLIP determination of vibrational entropy and heat capacity is neither accuracy-limiting nor time-limiting for our calculation of phase predominance diagrams.

2. The Sn-P-S ternary system as a case study

A variety of representations of the phase predominance diagrams are possible for ternary phosphosulfides, owing to the multivariate dependence of the Gibbs free energy on temperature and partial pressures of the two assumed reactant gases (P_2 and S_2). Fig. 6 a) shows phase predominance in the Sn-P-S system as a function of the partial pressures of P_2 and S_2 at a fixed temperature of 500 K. As an alternative representation, Fig. 6 b) and c) display phase predominance as a function of temperature and the partial pressure of either P_2 or S_2 , while the partial pressure of the other gas is held constant at 10^{-5} bar and 0.16 bar, respectively.

Binary Sn-S and Sn-P compounds appear in all displayed predominance diagrams. Additionally, the ternary compounds SnP_2S_8 , SnP_4S_{12} , SnP_2S_6 , and $SnPS_3$ are predicted to be the most stable phases under specific combinations of P_2 and S_2 partial pressures and temperatures. Of these ternary phosphosulfides, only $SnPS_3$ and SnP_2S_6 have been experimentally reported to date [38, 39]. A comparison between literature derived experimental synthesis conditions for these com-

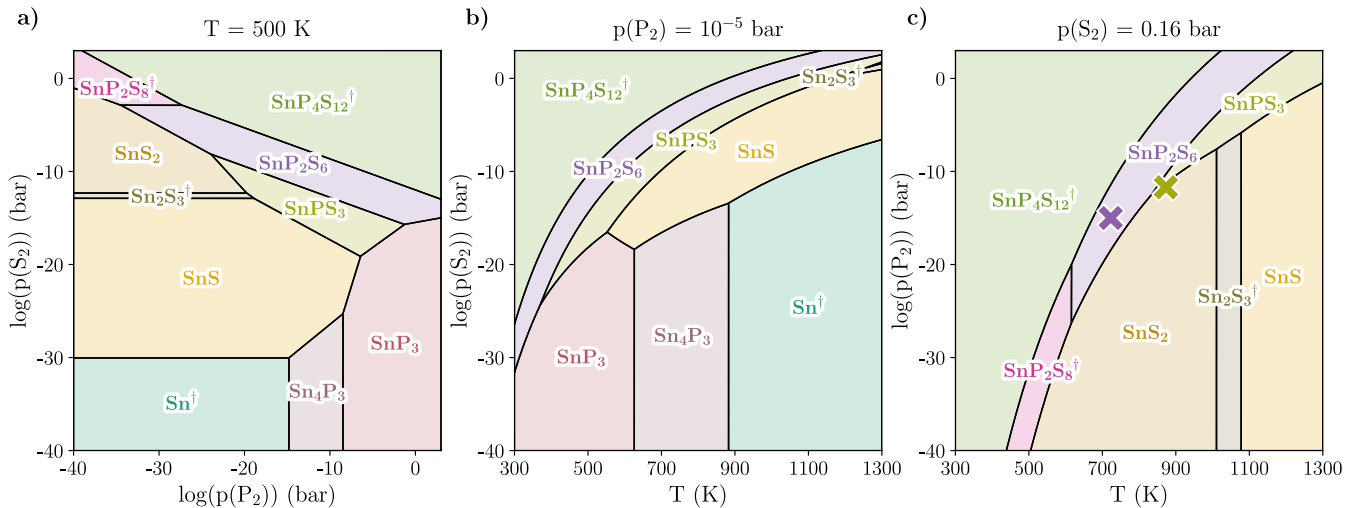


FIG. 6. Exemplary representations of phase predominance diagrams constructed for the Sn-P-S ternary system. a): Phase diagram for a constant temperature of 500 K in dependence of P_2 and S_2 partial pressures. b) and c): Phase diagrams dependent on temperature and P_2 and S_2 partial pressure, respectively, while the other is kept constant at 10^{-5} bar. Experimentally reported synthesis conditions of SnP_2S_6 and SnPS_3 [32, 33] are marked with crosses in c). The procedure used to extract these conditions from the literature is detailed in the SI. See caption of Fig. 2 for further details.

pounds [32, 33] and the predicted synthesizability windows shown in Fig. 6 c) gives remarkable agreement. While SnP_2S_6 and SnPS_3 have DFT formation enthalpies that lie on the stability hull ($E_h = 0$) of the Sn-P-S system, SnP_2S_8 and $\text{SnP}_4\text{S}_{12}$ are located approximately 50 meV/atom above the hull and are thus considered metastable at 0 K and expected to decompose. In contrast, SnP_2S_7 , which lies closer to the stability hull ($E_h \approx 32$ meV/atom), does not appear in the phase predominance diagrams shown in Fig. 6 and also exhibits imaginary phonon frequencies, indicating potential dynamic instability. These results emphasize again the importance of incorporating temperature-dependent thermodynamic properties when evaluating the experimental accessibility of predicted compounds.

3. Predicting phase transitions

Structural phase transitions between different polymorphs with the same composition can be predicted by our method. They can be attributed to differences in the temperature dependence of thermochemical properties in the polymorphs, leading to reordering of their Gibbs free energies. For our ternary phosphosulfide dataset, phase transitions are predicted for 55 compounds. For 19 of them, the transition occurs between 0 K and at room temperature. For the remaining 36, the transition occurs above room temperature. In general, the low-temperature polymorphs are often the ones that lie on the 0 K convex hull (lowest formation enthalpy structures). The high-temperature polymorphs are usually the ones with a higher entropic contribution to the Gibbs

free energy.

Fig. 7 shows exemplary phase diagrams including phase transitions. Since the pressure dependent contribution to the Gibbs free energy of reaction of each compound depends solely on the stoichiometry (see Eq. 11), the temperature of the phase transition is not pressure dependent.

In Fig. 7 a) the Ga-P-S system is displayed. At lower temperatures, tetragonal GaPS_4 , which lies on the stability hull at 0 K, is the most stable prototype. At around 450 K, tetragonal GaPS_4 is predicted to turn into a monoclinic structure ($E_h = 6$ meV/atom at 0 K). This agrees well with reports of monoclinic GaPS_4 synthesis at temperatures of 873-923 K [40].

Fig. 7 b) shows the Li-P-S system. Below 950 K, the enargite phase of Li_3PS_4 , which lies on the 0 K stability hull and has been experimentally reported [41], is predicted to be most stable. For higher temperatures, trigonal Li_3PS_4 ($E_h = 29$ meV/atom at 0 K) is predicted to be stabilized. The trigonal structural prototype has not been experimentally reported for Li_3PS_4 . Nonetheless, phase transitions have indeed been observed for Li_3PS_4 . A highly disordered α - Li_3PS_4 phase (not considered in this study due to disorder) has been reported for temperatures above 746 K [41, 42].

In Fig. 7 c), the Na-P-S system is shown. A phase transition is predicted for Na_2PS_3 at a transition temperature of around 650 K. Orthorhombic Na_2PS_3 , which is located on the zero-temperature stability hull, is predicted to be the most stable prototype in the low temperature regime. At an increased temperature Na_2PS_3 is expected to turn into a monoclinic structure ($E_h = 15$ meV/atom, space group $P2_1/c$). However, neither of these prototypes have been synthesized. While a phase transition at elevated

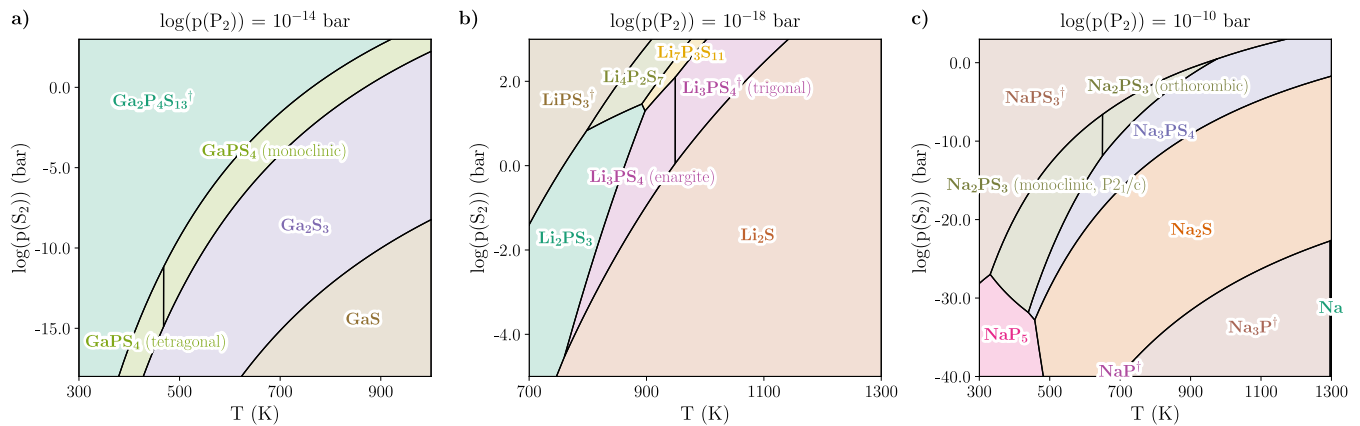


FIG. 7. Exemplary calculated phase predominance diagrams, predicting phase transitions between different polymorphs of the same composition (GaPS_4 , Li_3PS_4 , and Na_2PS_3).

temperatures (430 K) has indeed been experimentally reported for Na_2PS_3 [43], this transition occurs between two monoclinic phases.

4. Computational discovery of materials and their synthesizability windows

Finally, we show that our approach allows to combine the discovery of new materials and quantitative prediction of their synthesizability windows in a single workflow. In a 0 K DFT screening stage of ternary phosphosulfides, we identified 19 previously unknown phosphosulfide materials predicted to be on the zero-temperature convex hull [17]. A particularly interesting system is Hf-P-S, where we discovered four unreported Hf-P-S structures that lie on the stability hull, namely $\text{HfP}_4\text{S}_{12}$, HfP_2S_7 , HfP_2S_8 , and $\text{Hf}_2\text{P}_3\text{S}$. Only HfP_2S_6 had been experimentally and computationally reported in this material system prior to our work [44]. HfP_2S_6 lies 5 meV/atom above the stability hull. Fig. 8 shows a phase predominance diagram calculated for the Hf-P-S ternary system including these four new compounds. Three out of four are also predicted to be thermodynamically stable at finite temperatures over a range of partial pressures of the reactant gases. In addition, HfP_2S_6 is stabilized over a finite temperature window and a range of S_2 partial pressures in spite of its metastability at 0 K, consistent with its experimental observation.

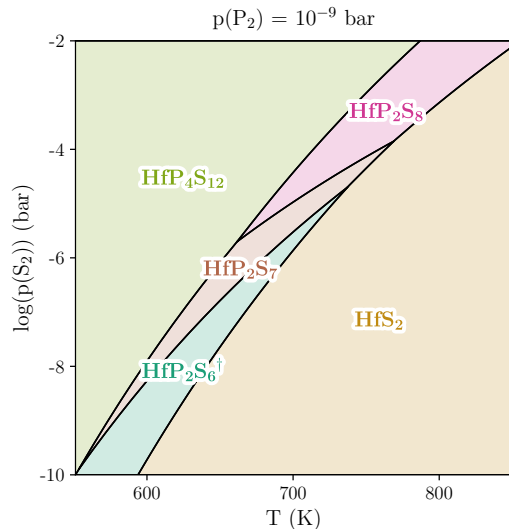


FIG. 8. Phase predominance diagram for the Hf-P-S ternary system showing temperature and partial pressure conditions under which the theoretically predicted $\text{HfP}_4\text{S}_{12}$, HfP_2S_7 , HfP_2S_8 and the experimentally reported HfP_2S_6 structures are predicted to be stable.

III. CONCLUSION AND OUTLOOK

We demonstrated an accelerated workflow to generate computational phase predominance diagrams for any inorganic material system. These diagrams are useful quantitative estimations of synthesizability windows of materials in a parameter space that is easily understood by experimentalists (temperature versus gas partial pressures). The key step enabling high-throughput predominance diagram generation was to determine vibrational entropy and heat capacity of materials from phonon band structures calculated via machine learned interatomic potentials (MLIP). Despite the semi-empirical nature of MLIP methods, our results indicate that they do not

compromise either the accuracy or the computational time needed to produce phase predominance diagrams based on DFT-calculated formation enthalpies.

Predominance diagrams generated in oxide, nitride, sulfide, and phosphide binary systems were generally consistent with experimental thermochemical data and experimentally reported synthesis conditions, highlighting chemical versatility. As expected, compounds that are metastable at 0 K are sometimes found to be thermodynamically stable under finite-temperature conditions, e.g., VO, V₃O₅, V₆O₁₁, and Cu₃P. In a similar fashion, materials lying on the convex stability hull at 0 K may no longer be stable at elevated temperatures.

As a high-throughput application of our method, we generated predominance diagrams for 48 distinct metal phosphosulfide ternary systems, comprising over 1000 ternary compounds and about 450 binaries. Some highlights were the identification of thermodynamically driven phase transitions between polymorphs, and the quantitative prediction of synthesis conditions for computationally discovered materials. These features are expected to facilitate communication between theorists and experimentalists, and between the computational and synthetic tasks of closed-loop autonomous labs for materials discovery. Future work could focus on the incorporation of configurational entropy, energy-lowering defects, and kinetic effects.

IV. METHODS

A. Data provenance

The phase predominance diagram of a generic binary or ternary system shows the solid phase with the lowest Gibbs free energy $\Delta G(T, p_i, p_j, \dots)$ among all considered phases in that system at each temperature T and gas partial pressure (p_i, p_j, \dots) coordinate point. The phases that are considered in the four chosen binary systems are the union of the material sets present on Materials Project [1], the Inorganic Crystal Structure Database (ICSD) [28], and a computational DFT database at the PBEsol level [27]. A full tabulated list of materials is given in the SI. The PBEsol database is also used for the crystal structures and enthalpies of elemental reference phases. For consistency, we relaxed all the considered entries from Materials Project and ICSD using the PBEsol functional. Potential ternary phosphosulfide (M-P-S) phases are taken from our own open-access computational database at the PBEsol level, containing about 1000 entries from a prototype-based screening study. [17]

The Gibbs free energy $\Delta G(T, p_i, p_j, \dots)$ for each considered material is calculated with the HSC Chemistry software package (Metso) [26]. Three thermochemical properties are required for each material: its entropy $S(298\text{ K})$ and formation enthalpy $\Delta H_f(298\text{ K})$ at room-temperature, and its temperature-dependent heat capacity $C_p(T)$. Calculation details for these three quantities

are given in the next sections.

B. Formation enthalpy by density functional theory with reference energy correction

All structures that do not originate from the general-purpose PBEsol database [27] or from our own PBEsol database of ternary phosphosulfides database [17] are relaxed using DFT. We employ the projector-augmented wave method [45] and the PBEsol functional [46] as implemented in the Vienna Ab-Initio Simulation Package (VASP) [47–51]. All structure relaxations are performed using a Γ -centered uniform k-points grid with 5 k-points per \AA^{-1} along each reciprocal lattice direction by setting the KSPACING tag in VASP to 0.22. An energy cutoff of at least 550 eV is selected. As convergence criteria, a difference of 10 meV/ \AA force on all atoms, and a difference of 10^{-6} eV/atom in total energy are chosen [17].

The enthalpy of formation of a given compound is defined as the difference between the compound’s zero-temperature total energy and the energies of its elemental components μ_i , weighted by their stoichiometric coefficients n_i .

$$\Delta H_f = E_{Total} - \sum_i n_i \mu_i \quad . \quad (1)$$

Even though a material’s zero-temperature formation enthalpy is directly available from a simple DFT structural relaxation of the material and of its elemental constituent phases, reproducing experimental formation enthalpies at room-temperature is a known challenge in materials science [52, 53]. A convenient approach to improve the formation enthalpy prediction is using fitted elemental-phase reference energies (FERE) [16]. In this method, corrections $\delta\mu_i^{FERE}$ are fitted to the total energies of each of the elemental reference phases to reproduce experimentally observed values of ΔH_f

$$\mu_i^{FERE} = \mu_i + \delta\mu_i^{FERE} \quad . \quad (2)$$

Values for these corrections are obtained by fitting the $\delta\mu_i^{FERE}$ correction for each element to minimize the difference between experimental and calculated ΔH_f ($\Delta H_f^{exp} - \Delta H_f^{calc}$) for all materials with available experimental formation enthalpies. The corrections for all elements are fitted simultaneously

$$\Delta H_f^{exp} - \Delta H_f^{calc} = \sum_i n_i \delta\mu_i^{FERE} \quad . \quad (3)$$

This requires a reference dataset containing both experimental values for the formation enthalpy and the corresponding DFT total energies for each of the compounds, raising the question of how to correctly compare experimental values (typically available at room temperature) with DFT value (at 0 K). It has been shown [52] that including the zero-point energy and enthalpic contributions

at finite temperatures in the calculation does not lead to a significant improvement of the formation enthalpy prediction. Thus, we simply use the DFT-calculated total energy at 0 K in the fitting of the elemental reference-phase energies.

Experimentally measured values for the formation enthalpy ΔH_f^{exp} are extracted from the HSC Chemistry experimental database which provides experimental $H(298\text{ K})$, $S(298\text{ K})$ and C_p data for about 30,000 species [26]. Four distinct sets of elemental reference phase energies are fitted separately using the FERE approach. The fitted energies are shown in Table I). The first set consists of 150 binary metal oxides, and it is used to plot the V-O phase diagram. the second set consists of 118 binary metal sulfides, and it is used to plot the Sn-S phase diagram. The third set includes binary metal phosphides (46) and nitrides (53), and is used to plot the Ta-N and Cu-P phase diagram. The reason for fitting nitrides and phosphides together is the scarcity of experimental thermochemical data for these classes of materials, and it may be justified by homovalence of N and P. The fourth dataset consists of metal phosphides (39) and metal sulfides (107), and includes 121 binaries, 21 ternaries, and 2 quaternaries.

Uncorrected DFT calculations tend to systematically overestimate ΔH_f (less negative) with respect to experiment. The mean absolute error (MAE) of the uncorrected formation enthalpies exceeds 150 meV/atom for all four datasets. After fitting reference phase energies, the MAE is significantly reduced to the 52-72 meV/atom range for all four datasets, comparable to previous work using the FERE method or similar correction schemes [54–56]. As a rule of thumb, experimental uncertainties in the determination of formation enthalpy are estimated to be around 40 meV/atom [25].

C. Entropy and heat capacity by machine-learned interatomic potentials

Room-temperature vibrational entropy $S(298\text{ K})$ and heat capacity C_p for each material are calculated employing the universal MLIP model MatterSim [13] combined with the phonopy package [57] using $20 \times 20 \times 20$ Monkhorst-Pack k-point meshes. $4 \times 4 \times 4$ supercells with atoms displaced by 0.01 Å are generated using phonopy and the resulting forces needed to calculate phonon frequencies and dispersion curves are predicted using MatterSim [13]. The temperature-dependent entropy $S(T)$ and constant-volume heat capacity $C_V(T)$ are derived from the Helmholtz free energy and harmonic phonon energy, respectively. These quantities are computed via summation over all calculated phonon modes. Although the quantity derived from the phonon band structure is the constant-volume heat capacity C_V , we assume $C_V \simeq C_p$ under the assumption of incompressible solids.

The room-temperature entropy $S(298\text{ K})$ and temperature dependent heat capacity $C_p(T)$ from 298 K to

1300 K in steps of 25 K are computed by phonopy for all considered DFT-relaxed crystal structures. In HSC Chemistry the temperature dependence of the heat capacity is described by the extended Kelley equation [58].

$$C_p(T) = A + BT \cdot 10^{-3} + \frac{C}{T^2} \cdot 10^5 + DT^2 \cdot 10^{-6} + \frac{E}{T^3} \cdot 10^8 + FT^3 \cdot 10^{-9} \quad (4)$$

Therefore, the temperature-dependent $C_p(T)$ obtained from the phonon calculation is fitted with the Kelley equation in the 298 K \rightarrow 1300 K range, and the resulting best-fit parameters A-F are then supplied to HSC Chemistry to calculate Gibbs free energies (see next section).

The room-temperature heat capacity and entropy values calculated for all binary compounds in the four datasets utilized in the fitting of the elemental reference-phase energy corrections are compared to the corresponding experimental values available in HSC Chemistry (389 binaries for entropy, 346 binaries for heat capacity). The MAEs are 0.042 meV/(atom·K) for $S(298\text{ K})$ and 0.043 meV/(atom·K) for $C_p(298\text{ K})$.

D. Calculation of Gibbs free energy and phase predominance diagrams by classical thermochemistry

Two-dimensional phase predominance diagrams are constructed in HSC Chemistry after extracting the temperature- and partial pressure-dependent Gibbs free energy $\Delta G(T, p_i, p_j, \dots)$ from the formation enthalpy and entropy at a single temperature, and the temperature-dependent heat capacity ($\Delta H_f(298\text{K})$, $S(298\text{K})$, and $C_p(T)$, respectively). Experimental predominance diagrams are based on the experimental values of these three quantities for the phases in the V-O, Ta-N, Sn-S, and Cu-P systems for which thermochemical data is available in HSC Chemistry. Computational diagrams are based on the DFT-calculated ΔH_f after applying the elemental reference phase correction, and on the MLIP-calculated $S(298\text{K})$, and $C_p(T)$. Assuming solids are incompressible, the dependence of the Gibbs free energy on the total pressure of the system can be neglected [4]. Hence, the temperature dependent Gibbs energy of a given compound is defined by

$$G(T) = H(T) - T \cdot S(T) \quad (5)$$

The temperature-dependent enthalpy $H(T)$ can be calculated from the formation enthalpy at a single temperature and the temperature-dependent heat capacity as

$$H(T) = \Delta H_f(298\text{K}) + \int_{298\text{K}}^T C_p(T) dT \quad (6)$$

The temperature-dependent entropy $S(T)$ can be derived with a similar procedure as

$$S(T) = S(298K) + \int_{298K}^T \frac{C_p(T)}{T} dT \quad (7)$$

The Gibbs energy of a compound (G_c) is then referenced to the Gibbs free energy of its elemental reference phases ($G_{i,r}$) as

$$\Delta G^0 = n_c G_c - \sum_i n_i G_{i,r} \quad (8)$$

with n_c the number of atoms in the compound and n_i the stoichiometric coefficient of the elemental constituents. The Gibbs free energy of each elemental phase G_i is calculated with Eq. 5, using the experimental $\Delta H_f(298K)$, $S(298K)$, and $C_p(T)$ values available in HSC Chemistry.

Finally, the Gibbs free energy dependence on the partial pressure of reactive gases is defined by the equilibrium constant K

$$K = \frac{a_c^{n_c}}{\prod_i a_{i,r}^{n_i}} \quad (9)$$

with a being the thermodynamic activity of the corresponding species and n the stoichiometric coefficient. For

gaseous substances, a is described by their effective partial pressure p and for pure substances in the solid state, a is equal to 1 [59, 60]. In this work, phase predominance diagrams are calculated depending on one or two partial pressures of the corresponding reactive gases (O_2 , N_2 , P_2 , S_2) and the metal activity is assumed to be 1 over the total temperature range. This implies that sublimation of metallic species during phase formation is neglected and may lead to an overestimation of the thermodynamic stability of metal-rich compounds at elevated temperatures, particularly for systems containing highly volatile metals.

The equilibrium constant K is connected to the Gibbs free energy by

$$\ln K = -\frac{\Delta G_R}{RT} \quad (10)$$

Hence, the total Gibbs free energy for a compound is extracted by combining Eq. 5 and Eq. 10 [26, 61]

$$\Delta G = \Delta G^0 + RT \ln K \quad (11)$$

The phase predominance diagrams are then constructed so that the compound with the minimal ΔG at a given temperature and partial pressure coordinate point is displayed.

-
- [1] A. Jain, S. P. Ong, G. Hautier, W. Chen, W. D. Richards, S. Dacek, S. Cholia, D. Gunter, D. Skinner, G. Ceder, and K. A. Persson, Commentary: The Materials Project: A materials genome approach to accelerating materials innovation, *APL Materials* **1**, 011002 (2013).
- [2] S. Kirklin, J. E. Saal, B. Meredig, A. Thompson, J. W. Doak, M. Aykol, S. Rühl, and C. Wolverton, The Open Quantum Materials Database (OQMD): Assessing the accuracy of DFT formation energies, *npj Computational Materials* **1**, 15010 (2015).
- [3] J. Schmidt, N. Hoffmann, H.-C. Wang, P. Borlido, P. J. M. A. Carrico, T. F. T. Cerqueira, S. Botti, and M. A. L. Marques, Machine-Learning-Assisted Determination of the Global Zero-Temperature Phase Diagram of Materials, *Advanced Materials (Deerfield Beach, Fla.)* **35**, e2210788 (2023).
- [4] P. Kayastha, G. Longo, and L. D. Whalley, A First-Principles Thermodynamic Model for the Ba-Zr-S System in Equilibrium with Sulfur Vapor, *ACS Applied Energy Materials* **7**, 11326 (2024).
- [5] A. Zunger, S.-H. Wei, L. G. Ferreira, and J. E. Bernard, Special quasirandom structures, *Physical Review Letters* **65**, 353 (1990).
- [6] J. J. Cordell, J. Pan, A. C. Tamboli, G. J. Tucker, and S. Lany, Probing configurational disorder in ZnGeN₂ using cluster-based Monte Carlo, *Physical Review Materials* **5**, 024604 (2021).
- [7] C. J. Bartel, S. L. Millican, A. M. Deml, J. R. Rumpitz, W. Tumas, A. W. Weimer, S. Lany, V. Stevanović, C. B. Musgrave, and A. M. Holder, Physical descriptor for the Gibbs energy of inorganic crystalline solids and temperature-dependent materials chemistry, *Nature Communications* **9**, 4168 (2018).
- [8] W. Sun and N. David, A critical reflection on attempts to machine-learn materials synthesis insights from text-mined literature recipes, *Faraday Discussions* **256**, 614 (2025).
- [9] J. Schlesinger, S. Hjaltason, N. J. Szymanski, and C. J. Bartel, Thermodynamic assessment of machine learning models for solid-state synthesis prediction, <https://arxiv.org/abs/2602.04075v1> (2026).
- [10] K. Tolborg and A. Walsh, Low-Cost Vibrational Free Energies in Solid Solutions with Machine Learning Force Fields, *The Journal of Physical Chemistry Letters* **14**, 11618 (2023).
- [11] S. Zhu, D. Sarıtürk, and R. Arróyave, Machine learning potentials for alloys: A detailed workflow to predict phase diagrams and benchmark accuracy, *npj Computational Materials* **11**, 340 (2025).
- [12] N. Unglert, M. Ketter, and G. K. H. Madsen, Active learning potentials for first-principles phase diagrams using replica-exchange nested sampling, *npj Computational Materials* **12**, 107 (2026).
- [13] H. Yang, C. Hu, Y. Zhou, X. Liu, Y. Shi, J. Li, G. Li, Z. Chen, S. Chen, C. Zeni, M. Horton, R. Pinsler, A. Fowler, D. Zügner, T. Xie, J. Smith, L. Sun, Q. Wang, L. Kong, C. Liu, H. Hao, and Z. Lu, *MatterSim: A Deep Learning Atomistic Model Across Elements, Temperatures and Pressures* (2024), [arXiv:2405.04967 \[cond-mat\]](https://arxiv.org/abs/2405.04967).
- [14] A. Loew, D. Sun, H.-C. Wang, S. Botti, and M. A. L. Marques, Universal machine learning interatomic potentials are ready for phonons, *npj Computational Materials*

- 11**, 178 (2025).
- [15] C. Comparotto, L. Whalley, K. Sopiha, R. J. W. Frost, T. Kubart, and J. J. S. Scragg, Thermodynamic insights into the Ba–S system for the formation of BaZrS₃ perovskites and other Ba sulfides, *Journal of Materials Chemistry A* **13**, 9983 (2025).
- [16] V. Stevanović, S. Lany, X. Zhang, and A. Zunger, Correcting density functional theory for accurate predictions of compound enthalpies of formation: Fitted elemental-phase reference energies, *Physical Review B* **85**, 115104 (2012).
- [17] J. S. Rodrigo, N. A. Kryger-Nelson, L. A. Mittmann, E. Bertin, I. E. Castelli, and A. Crovetto, AI-enhanced discovery and accelerated synthesis of metal phosphosulfides (2026), arXiv:2601.16693 [cond-mat].
- [18] I. Pallikara, P. Kayastha, J. M. Skelton, and L. D. Whalley, The physical significance of imaginary phonon modes in crystals, *Electronic Structure* **4**, 033002 (2022).
- [19] L. A. Burton, D. Colombara, R. D. Abellon, F. C. Grozema, L. M. Peter, T. J. Savenije, G. Dennler, and A. Walsh, Synthesis, Characterization, and Electronic Structure of Single-Crystal SnS, Sn₂S₃, and SnS₂, *Chemistry of Materials* **25**, 4908 (2013).
- [20] D. Mootz and H. Puhl, Die Kristallstruktur von Sn₂S₃, *Acta Crystallographica* **23**, 471 (1967).
- [21] J. P. Odile, S. Soled, C. A. Castro, and A. Wold, Crystal growth and characterization of the transition-metal phosphides copper diphosphide, nickel diphosphide, and rhodium triphosphide, *Inorganic Chemistry* **17**, 283 (1978).
- [22] H. Nowotny and E. Henglein, Ein Beitrag zur Kenntnis ternärer Phosphorlegierungen, *Monatshefte für Chemie und verwandte Teile anderer Wissenschaften* **79**, 385 (1948).
- [23] S. Westman, I. Lindqvist, B. Sparrman, G. B. Nielsen, H. Nord, and A. Jart, Note on a Phase Transition in VO₂, *Acta Chemica Scandinavica* **15**, 217 (1961).
- [24] F. Aebi, Phasenuntersuchungen im System Vanadin-Sauerstoff und die Krystallstruktur von V₁₂O₂₆, *Helvetica Chimica Acta* **31**, 8 (1948).
- [25] J. A. Pople, Quantum Chemical Models (Nobel Lecture), *Angewandte Chemie* **38**, 1894 (1999).
- [26] A. Roine, HSC Chemistry, Metso.
- [27] J. Schmidt, H.-C. Wang, T. F. T. Cerqueira, S. Botti, and M. A. L. Marques, A dataset of 175k stable and metastable materials calculated with the PBEsol and SCAN functionals, *Scientific Data* **9**, 64 (2022).
- [28] D. Zagorac, H. Müller, S. Ruehl, J. Zagorac, and S. Rehme, Recent developments in the Inorganic Crystal Structure Database: Theoretical crystal structure data and related features, *Journal of Applied Crystallography* **52**, 918 (2019).
- [29] A. Crovetto, T. Unold, and A. Zakutayev, Is Cu_{3–x}P a Semiconductor, a Metal, or a Semimetal?, *Chemistry of Materials* **35**, 1259 (2023).
- [30] A. Crovetto, D. Kojda, F. Yi, K. N. Heinselman, D. A. LaVan, K. Habicht, T. Unold, and A. Zakutayev, Crystallize It before It Diffuses: Kinetic Stabilization of Thin-Film Phosphorus-Rich Semiconductor CuP₂, *Journal of the American Chemical Society* **144**, 13334 (2022).
- [31] M. H. Møller and W. Jeitschko, Darstellung, Eigenschaften und Kristallstruktur von Cu₂P₇ und Strukturverfeinerungen von CuP₂ und AgP₂, *Zeitschrift für anorganische und allgemeine Chemie* **491**, 225 (1982).
- [32] J. He, S. H. Lee, F. Naccarato, G. Brunin, R. Zu, Y. Wang, L. Miao, H. Wang, N. Alem, G. Hautier, G.-M. Rignanese, Z. Mao, and V. Gopalan, SnP₂S₆: A Promising Infrared Nonlinear Optical Crystal with Strong Nonresonant Second Harmonic Generation and Phase-Matchability, *ACS Photonics* **9**, 1724 (2022).
- [33] G. Dittmar and H. Schäfer, Die Struktur des Di-Zinn-Hexathiohypodiphosphats Sn₂P₂S₆ / The Crystal Structure of Sn₂P₂Se, *Zeitschrift für Naturforschung B* **29**, 312 (1974).
- [34] W. Sun, S. T. Dacek, S. P. Ong, G. Hautier, A. Jain, W. D. Richards, A. C. Gamst, K. A. Persson, and G. Ceder, The thermodynamic scale of inorganic crystalline metastability, *Science Advances* **2**, e1600225 (2016).
- [35] R. Diehl and C.-D. Carpentier, The crystal structure of chromium thiophosphate, CrPS₄, *Acta Crystallographica Section B: Structural Crystallography and Crystal Chemistry* **33**, 1399 (1977).
- [36] W. F. Kuhs, R. Nitsche, and K. Scheunemann, The argyrodites — A new family of tetrahedrally close-packed structures, *Materials Research Bulletin* **14**, 241 (1979).
- [37] G. Ouvrard, R. Brec, and J. Rouxel, Structural determination of some MPS₃ layered phases (M = Mn, Fe, Co, Ni and Cd), *Materials Research Bulletin* **20**, 1181 (1985).
- [38] B. Scott, M. Pressprich, R. D. Willett, and D. A. Cleary, High temperature crystal structure and DSC of Sn₂P₂S₆, *Journal of Solid State Chemistry* **96**, 294 (1992).
- [39] Z. Wang, R. D. Willett, R. A. Laitinen, and D. A. Cleary, Synthesis and Crystal Structure of SnP₂S₆, *Chemistry of Materials* **7**, 856 (1995).
- [40] P. Buck and C. D. Carpentier, The crystal structure of gallium thiophosphate, GaPS₄, *Acta Crystallographica Section B Structural Crystallography and Crystal Chemistry* **29**, 1864 (1973).
- [41] K. Homma, M. Yonemura, T. Kobayashi, M. Nagao, M. Hirayama, and R. Kanno, Crystal structure and phase transitions of the lithium ionic conductor Li₃PS₄, *Solid State Ionics* **182**, 53 (2011).
- [42] K. Kaup, L. Zhou, A. Huq, and L. F. Nazar, Impact of the Li substructure on the diffusion pathways in alpha and beta Li₃PS₄: An in situ high temperature neutron diffraction study, *Journal of Materials Chemistry A* **8**, 12446 (2020).
- [43] T. Scholz, C. Schneider, R. Eger, V. Duppel, I. Moudrakovski, A. Schulz, J. Nuss, and B. V. Lotsch, Phase formation through synthetic control: Polymorphism in the sodium-ion solid electrolyte Na₄P₂S₆, *Journal of Materials Chemistry A* **9**, 8692 (2021).
- [44] A. Simon, H. Hahn, and K. Peters, Darstellung und Aufbau von HfP₂S₆ / Preparation of HfP₂S₆, *Zeitschrift für Naturforschung B* **40**, 730 (1985).
- [45] P. E. Blöchl, Projector augmented-wave method, *Physical Review B* **50**, 17953 (1994).
- [46] J. P. Perdew, A. Ruzsinszky, G. I. Csonka, O. A. Vydrov, G. E. Scuseria, L. A. Constantin, X. Zhou, and K. Burke, Restoring the Density-Gradient Expansion for Exchange in Solids and Surfaces, *Physical Review Letters* **100**, 136406 (2008).
- [47] G. Kresse and J. Hafner, Ab initio molecular dynamics for liquid metals, *Physical Review B* **47**, 558 (1993).
- [48] G. Kresse and J. Hafner, Ab initio molecular-dynamics simulation of the liquid-metal–amorphous-semiconductor transition in germanium, *Physical Review B* **49**, 14251

- (1994).
- [49] G. Kresse and J. Furthmüller, Efficiency of ab-initio total energy calculations for metals and semiconductors using a plane-wave basis set, *Computational Materials Science* **6**, 15 (1996).
- [50] G. Kresse and J. Furthmüller, Efficient iterative schemes for ab initio total-energy calculations using a plane-wave basis set, *Physical Review B* **54**, 11169 (1996).
- [51] G. Kresse and D. Joubert, From ultrasoft pseudopotentials to the projector augmented-wave method, *Physical Review B* **59**, 1758 (1999).
- [52] C. J. Bartel, Review of computational approaches to predict the thermodynamic stability of inorganic solids, *Journal of Materials Science* **57**, 10475 (2022).
- [53] A. Wang, R. Kingsbury, M. McDermott, M. Horton, A. Jain, S. P. Ong, S. Dwaraknath, and K. A. Persson, A framework for quantifying uncertainty in DFT energy corrections, *Scientific Reports* **11**, 15496 (2021).
- [54] Y. Zhang, D. A. Kitchaev, J. Yang, T. Chen, S. T. Dacek, R. A. Sarmiento-Pérez, M. A. L. Marques, H. Peng, G. Ceder, J. P. Perdew, and J. Sun, Efficient first-principles prediction of solid stability: Towards chemical accuracy, *npj Computational Materials* **4**, 9 (2018).
- [55] M. Pandey and K. W. Jacobsen, Heats of formation of solids with error estimation: The mBEEF functional with and without fitted reference energies, *Physical Review B* **91**, 235201 (2015).
- [56] S. Lany, Semiconductor thermochemistry in density functional calculations, *Physical Review B* **78**, 245207 (2008).
- [57] A. Togo, First-principles Phonon Calculations with Phonopy and Phono3py, *Journal of the Physical Society of Japan* **92**, 012001 (2023).
- [58] Chas. G. Maier and K. K. Kelley, An equation for the representation of high-temperature heat content data, *Journal of the American Chemical Society* **54**, 3243 (1932).
- [59] I. Mills, International Union of Pure and Applied Chemistry, and International Union of Pure and Applied Chemistry, eds., *Quantities, Units, and Symbols in Physical Chemistry*, 2nd ed. (Blackwell Scientific Publications ; CRC Press [distributor], Oxford ; Boston : Boca Raton, Fla, 1993).
- [60] M. B. Ewing, T. H. Lilley, G. M. Olofsson, M. T. Rätzsch, and G. Somsen, Iupac: A report of IUPAC commission 1.2 on thermodynamics: Standard quantities in chemical thermodynamics. Fugacities, activities, and equilibrium constants for pure and mixed phases, *The Journal of Chemical Thermodynamics* **27**, 1 (1995).
- [61] E. Epifano and D. Monceau, Ellingham diagram: A new look at an old tool, *Corrosion Science* **217**, 111113 (2023).